Random vibration analysis of axially compressed cylindrical shells under turbulent boundary layer in a symplectic system

Yuyin Li[a], Yahui Zhang[a*], David Kennedy[b]

[a] *State Key Laboratory of Structural Analysis for Industrial Equipment, Faculty of Vehicle Engineering and Mechanics, Dalian University of Technology, Dalian 116023, PR China;*

[b] *School of Engineering, Cardiff University, Cardiff CF24 3AA, Wales, UK*

Corresponding author:

Dr. Y. H. Zhang

State Key Laboratory of Structural Analysis for Industrial Equipment

Department of Engineering Mechanics, Faculty of Vehicle Engineering and Mechanics,

Dalian University of Technology, Dalian 116023, PR China

Email: zhangyh@dlut.edu.cn

Tel: +86 411 84706337

Fax: +86 411 84708393

Abstract

A random vibration analysis of an axially compressed cylindrical shell under a turbulent boundary layer (TBL) is presented in the symplectic duality system. By expressing the cross power spectral density (PSD) of the TBL as a Fourier series in the axial and circumferential directions, the problem of structures excited by a random distributed pressure due to the TBL is reduced to solving the harmonic response function, which is the response of structures to a spatial and temporal harmonic pressure of unit magnitude. The governing differential equations of the axially compressed cylindrical shell are derived in the symplectic duality system, and then a symplectic eigenproblem is formed by using the method of separation of variables. Expanding the excitation vector and unknown state vector in symplectic space, decoupled governing equations are derived, and then the analytical solution can be obtained. In contrast to the modal decomposition method (MDM), the present method is formulated in the symplectic duality system and does not need modal truncation, and hence the computations are of high precision and efficiency. In numerical examples, harmonic response functions for the axially compressed cylindrical shell are studied, and a comparison is made with the MDM to verify the present method. Then, the random responses of the shell to the TBL are obtained by the present method, and the convergence problems induced by Fourier series expansion are discussed. Finally, influences of the axial compression on random responses are investigated.

Key words: axially compressed cylindrical shell; turbulent boundary layer; symplectic duality system; random response

1 Introduction

Aircraft structures, such as launch vehicles and missiles, are inevitably excited by random pressure due to the turbulent boundary layer (TBL) on the outer surface of the structure. This excitation can cause low-amplitude vibration and eventually long-term structural fatigue. Meanwhile, the TBL is one of the main sources of noise, which may interfere with devices or reduce the comfort of aircraft passengers. For these reasons, the vibration of flexible structures under the TBL is of interest to many researchers and engineers.

The TBL is a classical distributed pressure excitation, which is intrinsically random in both the temporal and spatial domains. When studying random responses of structures subjected to the TBL, it is usual to consider it as a random pressure field, and a wavenumber-frequency cross power spectral density (PSD) is used to describe it. A widely used model of the TBL in the literature was introduced by Corcos [1], and was based on experimental observations and fitted empirically with some theoretical guidance. However, it overestimates the wall-pressure cross PSD at wavenumbers below the convective peak. Based on Corcos' model, Efimtsov [2] took into account the dependence of spatial correlation on boundary layer thickness and separation variables in his empirical model. Like Efimtsov, Smol'yakov and Tkachenko [3] added a correction to improve the prediction of Corcos' model at low wavenumber levels, without significantly affecting the convective peak levels. Graham [4] performed a comparative study for the sound radiated by a TBL driven plate, with a view to determining which model is most appropriate to noise problems in aircraft structures.

In order to provide strong capabilities for structural analysis with complex boundary conditions and geometric configurations, numerical methods such as the finite element method (FEM) are widely applied to vibration analysis of structures under the TBL [5-8]. Combining classical thin shell theory and the FEM, Lakis and Paidoussis [5] presented a hybrid finite element, in which displacement functions are determined from Sanders' shell equations instead of polynomial functions. This hybrid finite element was used for the prediction of random responses of a cylindrical shell to the TBL or arbitrary random pressure fields. Esmailzdeh et al. [6, 7] used the FEM to analyze the root mean square displacement responses of a flat rectangular plate [6] and curved thin shell [7]. Montgomery [8] developed a modelling process for aircraft structural-acoustic responses due to random sources. The analysis was based on using the FEM to represent the structure, coupled to a boundary element method (BEM) representation of the acoustic domains. Random excitations, including a diffuse field, a TBL noise and an engine shockcell noise, were considered in this analysis. However, the first basic step of FEM is the discretization of the random pressure field excited by the TBL, which means that the continuous random field is approximated by a finite number of random variables at nodal points. Since the correlation of two arbitrary random forces at nodal points must be considered in the analysis, the computation time is very sensitive to the number of elements. For example, in [6], when the number of elements increased 4 times, the computation time increased 90 times. Moreover, as the excitation frequency increases the wavelength of structural deformation decreases, and a very fine mesh with many elements is needed to accurately simulate the small wavelength deformation. Hence, the size of the FE model of the structure increases significantly which leads to more computation time, especially for the case excited by the TBL, which has a wide frequency band.

Except for using the FEM, responses to distributed random excitation such as the TBL are most often represented by a double integral over the structure, where the integrand is given by the cross PSD of the excitation and the Green's function of the structure. However, the double integral may result in large numerical computation time. To avoid computing the double integral directly, a Fourier series was introduced by Newland [9] and Lin [10] to expand the cross PSD of the TBL, so that the responses were derived as a double summation over the wavenumber domain. In this formulation, the problem of structures subjected to the TBL was reduced to solving the structure's harmonic response function, given as the deterministic response to a spatial and temporal harmonic pressure, and hence the computation complexity and time were reduced rapidly. Meanwhile, coefficients of the Fourier series can be obtained analytically for structures with regular shapes, such as beams, rectangular plates or cylindrical shells, and thus the computation time can be reduced further.

According to Newland [9] and Lin [10], the problem of a structure subjected to the TBL is reduced to solving the structure's harmonic response function, following which some standard method, such as the modal decomposition method (MDM) [11-16] can be used. Based on the MDM and the boundary integral formulation, Durant et al. [11] provided a numerical approach for vibroacoustic responses of a thin cylindrical pipe excited by a turbulent internal flow, and numerical results were compared to those of an experiment. Zhou et al. [12] used the MDM to investigate the sound transmission through a double-walled cylindrical shell lined with poroelastic material in the core, excited by the TBL. The sound wave propagating in the porous material was discussed in detail. Liu [13] extended an earlier deterministic method, using the MDM and the modal receptance method to predict the random noise transmission through curved aircraft panels with stringer and ring frame attachments. Combining the wavenumber approach and MDM, Maury et al. [14, 15] presented a self-contained analytical framework for determining the vibroacoustic responses of a plate to a large class of random excitations, such as an incidence diffuse acoustic field, a fully developed turbulent flow and a spatially uncorrelated pressure field. Convergence properties of the modal formulations in different load cases were examined. However, because the TBL has a wide frequency band, a large number of modes must be used in the MDM, and modal truncation may reduce the computational accuracy. Some researchers recommend that the cross modal terms may be neglected if certain conditions are satisfied [14], but others state that this approximation can produce a large error [17, 18]. Besides, some other approximate approaches are applied to reduce the computation of the MDM. For example, a scaling procedure named Asymptotical Scaled Modal Analysis (ASMA) was introduced by De Rosa and Franco [16] to reduce the computational cost of the MDM. ASMA is based on an assumption that the quadratic response depends on the number of modes resonating in a given frequency band and on the damping. On the other hand, for a cylindrical shell, the axial modes can be determined approximately by the modes of an equivalent beam with similar boundary conditions. Hence, modal shape functions of cylindrical shells are always described as the combination of axial beam functions and circumferential trigonometric functions. However, as pointed out by Lü and Chen [20], numerical instability may arise when calculating the modal shape functions with non-simply supported boundary conditions.

Apart from the MDM, other methods, such as the spectral finite element method (SFEM) [17, 21] and the dynamic stiffness method (DSM) [22] are also applied to the analysis of structures under the TBL. These methods are formulated in a Lagrangian system, and the variables are force or displacement. Based on a Hamiltonian system and symplectic state space theory, a new solution methodology for computational and analytical solid mechanics was introduced by Zhong [23]. Problems are described by the dual variable system, in which the basic equations are transformed to the symplectic duality system, and then a solution methodology such as the method of separation of variables and eigenfunction expansion follows. This solution methodology becomes rational, rather than the trial and error style semi-inverse approach. At present, the symplectic duality system has been successfully applied to the buckling analysis of cylindrical shells [24], the free vibration analysis of plates [25], the forced vibration and power flow analysis of plates [26, 27] and other problems. However, to the authors' knowledge, the symplectic duality system has not yet been used in the forced vibration analysis of cylindrical shells. This provides the initial motivation for the present work, in which this approach is also applied to the solution of random responses of cylindrical shells excited by the TBL.

The research object of this work is an axially compressed cylindrical shell under the TBL, in which the axial compression represents the temperature stress, air resistance or jet thrust on cylinder-like structures, such as launch vehicles and missiles. The work is structured as follows. In section 2, by way of a rigorous but simple derivation, the problem of structures subjected to the TBL is reduced to solving the harmonic response function. Then, in section 3, the governing equations of an axially compressed cylindrical shell subjected to a spatial and temporal harmonic pressure are converted into the symplectic duality system. Hence the method of separation of variables and the eigenfunction expansion method can be applied to obtain the analytical solution of the harmonic response function. Section 4 presents numerical examples. Firstly, harmonic response functions of structures are studied and a comparison between the present method and the MDM is made to verify the accuracy and efficiency of the former one. Influences of axial compression on the harmonic response functions are discussed. Subsequently, the present method is applied to the random vibration analysis of an axially compressed cylindrical shell excited by the TBL. The random responses are examined and are also compared to those of the MDM. Convergence of results and the influences of the axial compression on random response are investigated.

2 Random responses of structures subjected to TBL

Consider an axially compressed cylindrical shell subjected to the random pressure field $p(\mathbf{s},t)$ induced by the TBL, as shown in Fig. 1, where L is the length, R is the radius of the middle surface, h is the wall-thickness, $\mathbf{s}$ is the position of excitation and t is time. The arbitrary response of the structure can then be written in the convolution integral form

$$q(\mathbf{r},t) = \int_{\Gamma}\int_{0}^{t} h(\mathbf{r},\mathbf{s},t-\tau)p(\mathbf{s},\tau)\,\mathrm{d}\tau\mathrm{d}\mathbf{s} \tag{1}$$

where $\mathbf{r},\mathbf{s} = (x,\theta)$, $h(\mathbf{r},\mathbf{s},t-\tau)$ is the unit impulse response measured at a position $\mathbf{r}$ at time t due to a unit impulsive point load applied at a position $\mathbf{s}$ at time τ, and $\boldsymbol{\Gamma}$

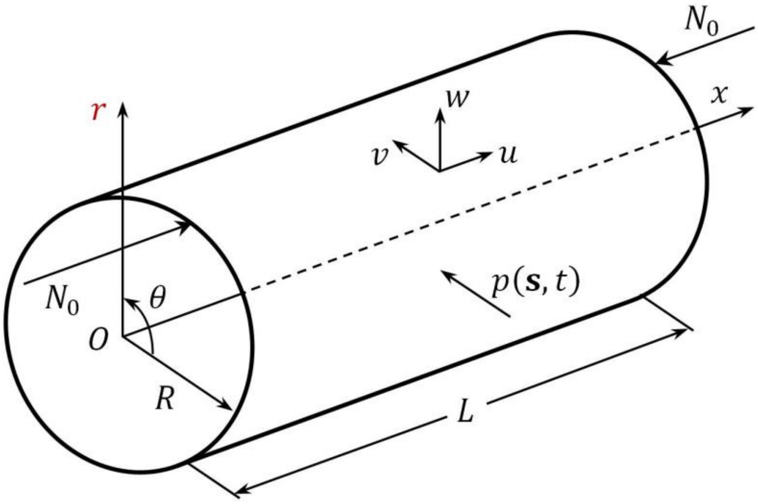

Fig. 1 Schematic of an axially compressed cylindrical shell

is the surface of the structure. $p(\mathbf{s},\tau)$ and $h(\mathbf{r},\mathbf{s},t-\tau)$ satisfy the causality conditions

$$\begin{aligned} &p(\mathbf{s},\tau)=0 \ \text{ for } \ \tau<0 \\ &h(\mathbf{r},\mathbf{s},t-\tau)=0 \ \text{ for } \ t<\tau \end{aligned} \tag{2}$$

By using Eq. (2), the integral with respect to τ in Eq. (1) can be expanded as

$$q(\mathbf{r},t)=\int_{\Gamma}\int_{-\infty}^{+\infty} h(\mathbf{r},\mathbf{s},t-\tau)p(\mathbf{s},\tau)\,\mathrm{d}\tau\mathrm{d}\mathbf{s} \tag{3}$$

By definition, since $q(\mathbf{r},t)$ is a random function in both the time and spatial domains, the cross-correlation function of responses of the structure at two points $\mathbf{r}_1$ and $\mathbf{r}_2$ can be written as

$$\begin{aligned} R_{qq}(\mathbf{r}_1,\mathbf{r}_2;t_1,t_2)&=\mathrm{E}[q(\mathbf{r}_1,t_1)q(\mathbf{r}_2,t_2)] \\ &=\int_{\Gamma}\int_{\Gamma}\int_{-\infty}^{+\infty}\int_{-\infty}^{+\infty} h(\mathbf{r}_1,\mathbf{s}_1,t_1-\tau_1)h(\mathbf{r}_2,\mathbf{s}_2,t_2-\tau_2)\mathrm{E}[p(\mathbf{s}_1,\tau_1)p(\mathbf{s}_2,\tau_2)] \end{aligned} \tag{4}$$

$$\mathrm{d}\tau_1\mathrm{d}\tau_2\mathrm{d}\mathbf{s}_1\mathrm{d}\mathbf{s}_2$$

where $\mathrm{E}[\quad]$ is the expectation operator, and hence $\mathrm{E}[p(\mathbf{s}_1,\tau_1)p(\mathbf{s}_2,\tau_2)]$ represents the cross-correlation function of the pressure field $p(\mathbf{s},t)$, which can be denoted as $R_{pp}(\mathbf{s}_1,\mathbf{s}_2;\tau_1,\tau_2)$. It is assumed that $p(\mathbf{s},t)$ is homogeneous in space and stationary in time, so that $R_{pp}(\mathbf{s}_1,\mathbf{s}_2,\tau_1,\tau_2)$ depends only on the time and space separation $\tau=\tau_2-\tau_1$ and $\boldsymbol{\xi}=\mathbf{s}_2-\mathbf{s}_1$ and can be denoted as $R_{pp}(\boldsymbol{\xi},\tau)$. By applying the Wiener-Khinchin theorem,

$$R_{pp}(\boldsymbol{\xi},\tau)=\int_{-\infty}^{+\infty}S_{pp}(\boldsymbol{\xi},\omega)\mathrm{e}^{\mathrm{i}\omega\tau}\,\mathrm{d}\omega \tag{5}$$

in which $S_{pp}(\boldsymbol{\xi},\omega)$ is the cross PSD of the TBL and ω is circular frequency. Substituting Eq. (5) into Eq. (4) gives

$$R_{qq}(\mathbf{r}_1,\mathbf{r}_2,\tau) = \int_{\Gamma}\int_{\Gamma}\int_{-\infty}^{+\infty}H(\mathbf{r}_1,\mathbf{s}_1,\omega)\big(H(\mathbf{r}_2,\mathbf{s}_2,\omega)\big)^{*}S_{pp}(\boldsymbol{\xi},\omega)\mathrm{e}^{\mathrm{i}\omega\tau}\,\mathrm{d}\omega\mathrm{d}\mathbf{s}_1\mathrm{d}\mathbf{s}_2 \tag{6}$$

in which superscript * denotes complex conjugate and

$$H(\mathbf{r},\mathbf{s},\omega)=\int_{-\infty}^{+\infty}h(\mathbf{r},\mathbf{s},t)\mathrm{e}^{-\mathrm{i}\omega t}\,\mathrm{d}t \tag{7}$$

is the frequency response function which gives the steady-state harmonic response at $\mathbf{r}$ as a result of unit amplitude harmonic excitation at frequency ω applied at $\mathbf{s}$.

A common semi-empirical model of the cross PSD of the TBL is attributed to Corcos

[1] as

$$S_{pp}(\boldsymbol{\xi},\omega)=\Phi_{pp}(\omega)\mathrm{e}^{-c_\theta R\omega|\xi_\theta|/U_c}\mathrm{e}^{-c_x\omega|\xi_x|/U_c}\mathrm{e}^{-\mathrm{i}\omega\xi_x/U_c} \tag{8}$$

where $\Phi_{pp}(\omega)$ is the auto PSD of the wall pressure, c_θ and c_x are constants describing the spatial coherence of the wall pressure field in the circumferential and axial directions, respectively, $\xi_\theta=\theta_2-\theta_1$ and $\xi_x=x_2-x_1$ is the distance between two points, and U_c is the convection velocity. According to [9, 10], the cross PSD $S_{pp}(\boldsymbol{\xi},\omega)$ can be expressed as combinations of an exponential Fourier series in the axial direction and a trigonometric Fourier series in the circumferential direction, as follows,

$$S_{pp}(\boldsymbol{\xi},\omega)=\Phi_{pp}(\omega)\sum_{M=-\infty}^{\infty}S_{ppx}(M)\mathrm{e}^{\mathrm{i}\alpha_M\xi_x}\sum_{N=1}^{\infty}S_{pp\varphi}(N)\cos(N\xi_\theta) \tag{9}$$

in which M and N are wavenumbers and $\alpha_M=\pi M/L$. The distances ξ_x and ξ_θ range from $-L$ to L and $-\pi$ to π, respectively, and thus the integrals of $S_{ppx}(M)$ and $S_{pp\varphi}(N)$ are reduced to finite intervals, i.e.,

$$\begin{aligned}
S_{ppx}(M)&=\frac{1}{2L}\int_{-L}^{L}\mathrm{e}^{-c_x\omega|\xi_x|/U_c}\mathrm{e}^{\mathrm{i}\omega\xi_x/U_c}\mathrm{e}^{-\mathrm{i}\alpha_M\xi_x}\,\mathrm{d}\xi_x\\
&=\frac{1}{2L}\left(\frac{1-\mathrm{e}^{-d_1L}}{d_1}+\frac{\mathrm{e}^{d_2L}-1}{d_2}\right)\\
S_{pp\theta}(N)&=\frac{1}{\pi}\int_{-\pi}^{\pi}\mathrm{e}^{-c_\theta R\omega|\xi_\theta|/U_c}\cos(N\xi_\theta)\,\mathrm{d}\xi_\theta=\frac{1}{\pi}\left(\frac{\mathrm{e}^{d_3\pi}-1}{d_3}+\frac{\mathrm{e}^{d_4\pi}-1}{d_4}\right)\\
d_1&=\frac{c_x\omega}{U_c}+\frac{\mathrm{i}\omega}{U_c}-\mathrm{i}\alpha_M,\ d_2=-\frac{c_x\omega}{U_c}+\frac{\mathrm{i}\omega}{U_c}-\mathrm{i}\alpha_M
\end{aligned} \tag{10}$$

$$d_3 = -\frac{Rc_\theta\omega}{U_c} + \mathrm{i}N,\ \ d_4 = -\frac{Rc_\theta\omega}{U_c} - \mathrm{i}N$$

Substituting Eq. (9) into Eq. (6) gives

$$R_{qq}(\mathbf{r}_1, \mathbf{r}_2, \tau) = \int_{-\infty}^{+\infty} \sum_{M=-\infty}^{+\infty} \sum_{N=1}^{+\infty} S_{ppx}(M) S_{pp\varphi}(N) G_{MN}(\mathbf{r}_1, \omega) \left(G_{MN}(\mathbf{r}_2, \omega)\right)^* \Phi_{pp}(\omega) \mathrm{e}^{\mathrm{i}\omega\tau}\,\mathrm{d}\omega \tag{11}$$

where

$$G_{MN}(\mathbf{r}, \omega) = \int_{\Gamma} \mathrm{e}^{\mathrm{i}\alpha_M x} \cos(N\theta) H(\mathbf{r}, \mathbf{s}, \omega)\,\mathrm{d}\mathbf{s} \tag{12}$$

is the harmonic response function, given as the response to a spatial and temporal harmonic pressure $p_{MN}(\mathbf{s}, t) = \mathrm{e}^{\mathrm{i}\alpha_M x} \cos(N\theta) \mathrm{e}^{\mathrm{i}\omega t}$. By applying the Wiener-Khinchin theorem to Eq. (11), the PSD of $q(\mathbf{r}, t)$ is obtained as

$$S_{qq}(\mathbf{r}_1, \mathbf{r}_2, \omega) = \sum_{M=-\infty}^{+\infty} \sum_{N=1}^{+\infty} S_{ppx}(M) S_{pp\varphi}(N) G_{MN}(\mathbf{r}_1, \omega) \left(G_{MN}(\mathbf{r}_2, \omega)\right)^* \Phi_{pp}(\omega) \tag{13}$$

In Eqs. (11) and (13), by assuming $\mathbf{r} = \mathbf{r}_1 = \mathbf{r}_2$, the auto correlation function and PSD of $q(\mathbf{r}, t)$ are obtained.

Thus, the problem of structures subjected to TBL can be reduced to solving the structure's harmonic response function, through expanding the auto PSD of the TBL as a Fourier series.

3 Solution of harmonic response functions in symplectic duality system

3.1 Governing equations

It is now assumed that all quantities vary harmonically with time as $e^{i\omega t}$ and this explicit dependence will henceforth be suppressed for simplicity. Based on Kirchhoff-Love shell theory [19], governing equations of an axially compressed cylindrical shell subject to the spatial and temporal harmonic pressure can be expressed as

$$\begin{gathered}\frac{\partial N_x}{\partial x}+\frac{1}{R}\frac{\partial N_{x\theta}}{\partial \theta}+\rho h\omega^2 u=0\\ \frac{\partial N_{x\theta}}{\partial x}+\frac{1}{R}\frac{\partial N_{\theta}}{\partial \theta}+\frac{1}{R}\frac{\partial M_{x\theta}}{\partial x}+\frac{1}{R^2}\frac{\partial M_{\theta}}{\partial \theta}+\rho h\omega^2 v=0\\ \frac{\partial^2 M_x}{\partial x^2}+\frac{2}{R}\frac{\partial^2 M_{x\theta}}{\partial x\,\partial \theta}+\frac{1}{R^2}\frac{\partial^2 M_{\theta}}{\partial \theta^2}-\frac{N_\theta}{R}+N_0\frac{\partial^2 w}{\partial x^2}+p_{MN}+\rho h\omega^2 w=0\end{gathered} \tag{14}$$

where ρ is the mass density, N_0 is the axial compression per unit length, u, v and w denote the displacements of the middle surface in the x, θ, and z directions, respectively, which do not vary through the thickness.

$$N_x=K\left[\frac{\partial u}{\partial x}+\frac{\nu}{R}\left(\frac{\partial v}{\partial \theta}+w\right)\right] \tag{15}$$

$$N_\theta=K\left[\frac{1}{R}\left(\frac{\partial v}{\partial \theta}+w\right)+\nu\frac{\partial u}{\partial x}\right] \tag{16}$$

$$N_{x\theta} = K\frac{1-\nu}{2}\left(\frac{\partial v}{\partial x} + \frac{1}{R}\frac{\partial u}{\partial \theta}\right) \tag{17}$$

are internal forces, in which $K = (1 + \mathrm{i}\eta)Eh/(1-\nu^2)$ is the in-plane rigidity, where E is Young's modulus, ν is Poisson's ratio, and η is the damping loss factor.

$$M_x = D\left[-\frac{\partial^2 w}{\partial x^2} + \frac{\nu}{R^2}\left(\frac{\partial v}{\partial \theta} - \frac{\partial^2 w}{\partial \theta^2}\right)\right] \tag{18}$$

$$M_\theta = D\left[\frac{1}{R^2}\left(\frac{\partial v}{\partial \theta} - \frac{\partial^2 w}{\partial \theta^2}\right) - \nu\frac{\partial^2 w}{\partial x^2}\right] \tag{19}$$

$$M_{x\theta} = D\frac{1-\nu}{2R}\left(\frac{\partial v}{\partial x} - 2\frac{\partial^2 w}{\partial x\,\partial \theta}\right) \tag{20}$$

are internal bending or twisting moments, where $D = (1 + \mathrm{i}\eta)Eh^3/12(1-\nu^2)$ is the flexural rigidity. The equivalent Kirchhoff in-plane and transversal shear forces are

$$S_x = N_{x\theta} + \frac{M_{x\theta}}{R} \tag{21}$$

$$V_x = \frac{\partial M_x}{\partial x} + \frac{2}{R}\frac{\partial M_{x\theta}}{\partial \theta} \tag{22}$$

The rotation of the shell can be defined as

$$\phi = -\frac{\partial w}{\partial x} \tag{23}$$

Eqs. (14)-(23) can be expressed in matrix form as

$$\frac{\partial \mathbf{z}}{\partial x} = \mathbf{H}\mathbf{z} + \mathbf{f} \tag{24}$$

where $\mathbf{z} = \{u, v, w, \phi, N_x, -S_x, V_x + N_0\phi, M_x + N_0 w\}^{\mathrm{T}}$ is the state vector in the symplectic space and $\mathbf{z}$ is a function of both x and θ, $\mathbf{H}$ is the Hamiltonian matrix operator given in the Appendix, $\mathbf{f} = \{0,0,0,0,0,0, p_{MN}, 0\}^{\mathrm{T}}$ is the excitation vector, and superscript T denotes transposition.

3.2 Separation of variables and symplectic eigenproblem

Taking no account of the excitation vector $\mathbf{f}$, Eq. (24) becomes a homogeneous equation, and hence it is natural to apply the method of separation of variables to reduce it to a differential eigenvalue problem. Therefore, the state vector can be expressed as

$$\mathbf{z} = \boldsymbol{\eta} \mathrm{e}^{\mu x} \tag{25}$$

Substituting Eq. (25) into Eq. (24) gives the symplectic eigenproblem

$$\mathbf{H}\boldsymbol{\eta} = \mu\boldsymbol{\eta} \tag{26}$$

From Eqs. (25) and (26), it can be concluded that the eigenvector $\boldsymbol{\eta}$ and eigenvalue μ characterize the vibration state of the shell. According to the periodic boundary conditions in the circumferential direction, $\boldsymbol{\eta}$ can be expressed as

$$\boldsymbol{\eta} = \mathbf{E}_n \boldsymbol{\psi}_n \tag{27}$$

where $\boldsymbol{\psi}_n$ is a constant vector which is independent of θ, and

$$\mathbf{E}_n = \mathrm{diag}[\bar{\mathbf{E}} \quad \bar{\mathbf{E}}]$$
$$\bar{\mathbf{E}} = \mathrm{diag}[\cos(n\theta), \sin(n\theta), \cos(n\theta), \cos(n\theta)] \tag{28}$$

and diag[ ] denotes a diagonal matrix.

Substituting Eq. (27) into Eq. (26) gives

$$\bar{\mathbf{H}}_n \boldsymbol{\psi}_n = \mu_n \boldsymbol{\psi}_n \tag{29}$$

where $\bar{\mathbf{H}}_n$ is a constant matrix which is only dependent on the structural parameters, the circumferential wavenumber n and the excitation frequency ω.

According to [23], the eigenvalues of matrix $\bar{\mathbf{H}}_n$ come in pairs μ_n and $-\mu_n$. In the subsequent analysis, the eigenvalues need to be sequenced according to the adjoint symplectic orthogonal relation, i.e.

$$\mu_{n,1}, \mu_{n,2}, \mu_{n,3}, \mu_{n,4}, -\mu_{n,1}, -\mu_{n,2}, -\mu_{n,3}, -\mu_{n,4} \tag{30}$$

Meanwhile, rearranging the associated eigenvector in the same order gives an eigenmatrix $\boldsymbol{\phi}_n$ with the following adjoint symplectic orthogonal relations

$$\int_0^{2\pi} \boldsymbol{\phi}_i^{\mathrm{T}} \mathbf{J}_8 \boldsymbol{\phi}_j \mathrm{d}\theta = \begin{cases} \mathbf{J}_8 & i = j \\ \mathbf{0}_8 & i \neq j \end{cases} \tag{31}$$

where $\mathbf{J}_8 = \begin{bmatrix} \mathbf{0} & \mathbf{I}_4 \\ -\mathbf{I}_4 & \mathbf{0} \end{bmatrix}$ is an eighth-order unit symplectic matrix which satisfies $\mathbf{J}_8^{\mathrm{T}} = -\mathbf{J}_8$, $\mathbf{I}_4$ and $\mathbf{0}_8$ are fourth-order unit and eighth-order zero matrices, respectively.

Expanding $\mathbf{z}$ and $\mathbf{f}$ in the orthogonal basis composed by $\boldsymbol{\phi}_n$, it is found that

$$\mathbf{z} = \sum_{n=1}^{+\infty} \boldsymbol{\phi}_n \mathbf{a}_n , \qquad \mathbf{f} = \sum_{n=1}^{+\infty} \boldsymbol{\phi}_n \mathbf{b}_n \tag{32}$$

where $\mathbf{a}_n$ and $\mathbf{b}_n$ are components of $\mathbf{z}$ and $\mathbf{f}$, respectively, in the basis. Considering the adjoint symplectic orthogonal relations shown in Eq. (31), $\mathbf{b}_n$ is obtained as

$$\mathbf{b}_n = -\mathbf{J}_8 \int_0^{2\pi} \boldsymbol{\phi}_n^{\mathrm{T}} \mathbf{J}_8 \mathbf{f} \mathrm{d}\theta \tag{33}$$

Since the spatial and temporal harmonic pressure p_{MN} has a trigonometric distribution as $\cos(N\theta)$ in the circumferential direction, it can be proved that $\mathbf{b}_n$ in Eq. (33) is a non-zero vector if and only if $n = N$, which means the summation in Eq. (32) needs no truncation. With this property, the computation of the present method can be reduced significantly.

Substituting Eq. (32) into Eq. (24) and considering the adjoint symplectic orthogonal relations again, it is found that

$$\frac{\mathrm{d}\mathbf{a}_n}{\mathrm{d}x} = \boldsymbol{\Phi}_n \mathbf{a}_n + \mathbf{b}_n \tag{34}$$

where $\boldsymbol{\Phi}_n = \mathrm{diag}\left[\mu_{n,1}, \mu_{n,2}, \cdots, -\mu_{n,4}\right]$ is a diagonal matrix in which elements are the eigenvalues, and hence Eq. (34) denotes eight decoupled inhomogeneous differential equations. Considering the exponential distribution of p_{MN} in the axial direction, the solutions of Eq. (34) can be expressed as the sum of inhomogeneous particular solutions and homogeneous general solutions, as

$$\mathbf{a}_n = \mathbf{B}_n\mathbf{A}_n - (\mathrm{i}\alpha_M\mathbf{I}_8 + \mathbf{\Phi}_n)^{-1}\mathbf{b}_n \tag{35}$$

where $\mathbf{B}_n = \mathrm{diag}[\mathrm{e}^{\mu_{n,1}x}, \mathrm{e}^{\mu_{n,2}x}, \cdots, \mathrm{e}^{-\mu_{n,4}x}]$ and $\mathbf{A}_n$ is a vector of undetermined coefficients, which can be determined by satisfying the boundary conditions. It is noted that since the calculations of exponent values $\mathrm{e}^{\mu_n x}$ are involved in the matrix $\mathbf{B}_n$, there might be a singularity problem in procedures of the present method when real parts of $\mu_n x$ are too large. However, the difficulty can be overcome through increasing the calculation precision.

3.3 Boundary conditions

The cylindrical shell has four displacement constraints (u, v, w, ϕ) and four force constraints (N_x, S_x, V_x, M_x) at the cross section. Combinations of the eight constraints can present any classical boundary conditions. It should be noted that any displacement constraint and the corresponding force constraint cannot coexist simultaneously, and hence each end of the cylindrical shell has only four displacement or force constraints.

The boundary conditions can be expressed as

$$\mathbf{\Upsilon}\mathbf{z}(x, \theta) = \mathbf{\Upsilon}\boldsymbol{\phi}_n\mathbf{a}_n(x) = \mathbf{0}_{8\times1} \tag{36}$$

where $\mathbf{\Upsilon}$ is an eighth-order diagonal matrix indicating the boundary conditions, e.g., for a simply support, $v = w = N_x = M_x = 0$, and hence

$$\boldsymbol{\Upsilon} = \mathrm{diag}[0,1,1,0,1,0,0,1] \tag{37}$$

Pre-multiplying both sides of Eq. (36) by $\boldsymbol{\Phi}_n^{\mathrm{T}}\mathbf{J}_8$ and integrating from 0 to 2π,

$$\begin{aligned} \int_0^{2\pi} \boldsymbol{\Phi}_n^{\mathrm{T}}\mathbf{J}_8\boldsymbol{\Upsilon}_{\mathrm{L}}\boldsymbol{\Phi}_n\, \mathbf{a}_n(0)\mathrm{d}\theta = \mathbf{0}_{8\times1} \\ \int_0^{2\pi} \boldsymbol{\Phi}_n^{\mathrm{T}}\mathbf{J}_8\boldsymbol{\Upsilon}_{\mathrm{R}}\boldsymbol{\Phi}_n\, \mathbf{a}_n(L)\mathrm{d}\theta = \mathbf{0}_{8\times1} \end{aligned} \tag{38}$$

where subscripts L and R denote the left and right ends of the cylindrical shell, respectively. Eq. (38) consists of eight independent equations, and after substituting Eq. (35) into it, the vector of undetermined coefficients $\mathbf{A}_n$ can be determined. It is worthwhile to point out that the only difference for different boundary conditions in the framework of the present method is the permutation of 1 and 0 in $\boldsymbol{\Upsilon}$, and hence it is convenient to expand the present method to other types of boundary conditions.

4 Numerical examples

The PSD of an arbitrary response is expressed by Eq. (13) as the combination of $G_{MN}(\mathbf{r},\omega)$, $S_{ppx}(M)$, $S_{pp\varphi}(N)$, and $\Phi_{pp}(\omega)$, in which $G_{MN}(\mathbf{r},\omega)$ is only dependent on the excitation frequency, structural parameters and boundary conditions, whereas $S_{ppx}(M)$, $S_{pp\varphi}(N)$ and $\Phi_{pp}(\omega)$ are only related to the TBL model. Therefore, the effectiveness of the present method may be affected by two aspects, firstly the solution of $G_{MN}(\mathbf{r},\omega)$, and secondly the convergence problem introduced by the Fourier series expansion. Hence the validation and discussion of the present method will be focused on these two aspects. Furthermore, considering that variation of the axial compression will change the dynamic characteristics of the cylindrical shell, the influences of axial compression on random responses are investigated by the present method.

In the numerical examples, the present method is applied to obtaining the random responses of a type of rocket body, which is made of high-strength alloy steels. The rocket body is simplified as a cylindrical shell with properties as follows: length $L = 5\text{m}$, radius of the middle surface $R = 0.5\text{m}$, wall thickness $h = 0.01\text{m}$, mass density $\rho = 7850\ \text{kg/m}^3$, Young's modulus $E = 215$ GPa, Poisson's ratio $\nu = 0.32$, and damping loss factor $\eta = 0.01$. Since the boundary conditions at the two ends have no essential influence on the performance of the present method, for the sake of brevity, results are given for the simply supported case unless specified otherwise.

4.1 Harmonic response functions

4.1.1 Comparisons of the present method and MDM

The analytical solution of the harmonic response function is obtained by the present method in the symplectic duality system of section 3. To validate the expression derived above and to develop an understanding for the advantage of the present method, the responses of a cylindrical shell are investigated and the results are compared to those of the MDM.

The MDM for the vibration analysis of a cylindrical shell can be found in [19], and is omitted here for simplicity. It should be pointed out that modal shape functions of cylindrical shells are always described as the combination of axial beam functions and circumferential trigonometric functions. For simply supported boundary conditions the circumferential modes have forms of $\sin(n\theta)$ or $\cos(n\theta)$, and the axial modes have forms of $\sin\left(\frac{\pi m x}{L}\right)$. Considering the spatial distribution of p_{MN} and the orthogonality of modes, it can be concluded that: (i) the nth order modal response is zero except if $n = N$; (ii) the mth order modal response is zero except if $m = M$ or $m + M$ is odd. With this property, the number of participant modes decreases and hence the computation of the MDM can be reduced.

In order to acquire a preliminary understanding of the dynamic characteristics of the cylindrical shell, a modal analysis is first performed. The natural frequencies of orders $n \leq 5$ and $m \leq 10$ are listed in Table 1, where the axial compression N_0 is equal to zero.

Figs. 2 and 3 show the harmonic response functions $G_{MN}(\mathbf{r}, \omega)$ corresponding to the displacement w and bending moment M_x, respectively, calculated by the present method and the MDM. The following results are given at point $\mathbf{r}$ with co-ordinates $x = 0.3L$ and $\theta = 0.4\pi$, if not otherwise stated. Due to the resonance and the small damping used in this work, each peak of $G_{MN}(\mathbf{r}, \omega)$, as shown in Fig. 2, matches one undamped natural frequency. Comparing these peaks with the results in Table 1, the orders can be determined and indicated as (m, n) in Fig. 2. For the case of $M = 1$ and $N = 2$, only modes with order $n = 2$ in the circumferential direction and $m = 1$ or an even integer in the axial direction are excited. For the case of $M = 4$ and $N = 4$, a similar phenomenon can be observed.

Table 1 Natural frequencies of the cylindrical shell without axial compression

f_{mn}(Hz)		$n =$				
		1	2	3	4	5
$m =$	1	100	44	77	143	231
	2	315	132	100	150	234
	3	553	261	159	171	244
	4	776	407	243	210	262
	5	968	555	341	265	290
	6	1122	694	445	333	328
	7	1238	820	548	408	375
	8	1323	931	648	486	430
	9	1385	1027	743	565	489
	10	1431	1109	830	643	552

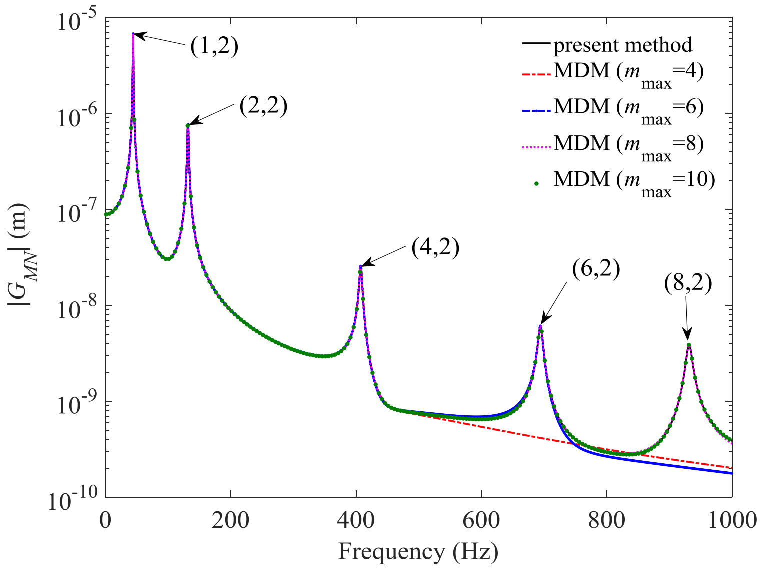

(a) $M = 1, N = 2$

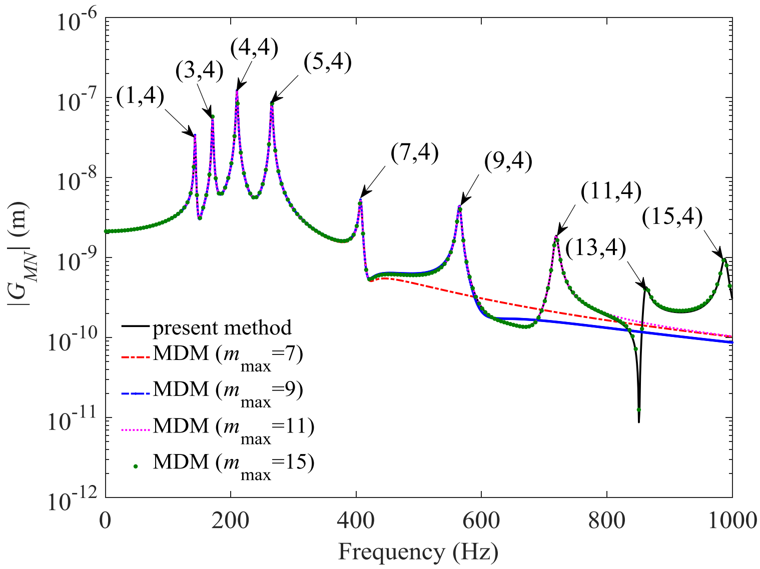

(b) $M = 4, N = 4$

Fig. 2 Magnitudes of the harmonic response function corresponding to the displacement w at $(0.3L, 0.4\pi)$, calculated by the present method and the MDM with different truncations

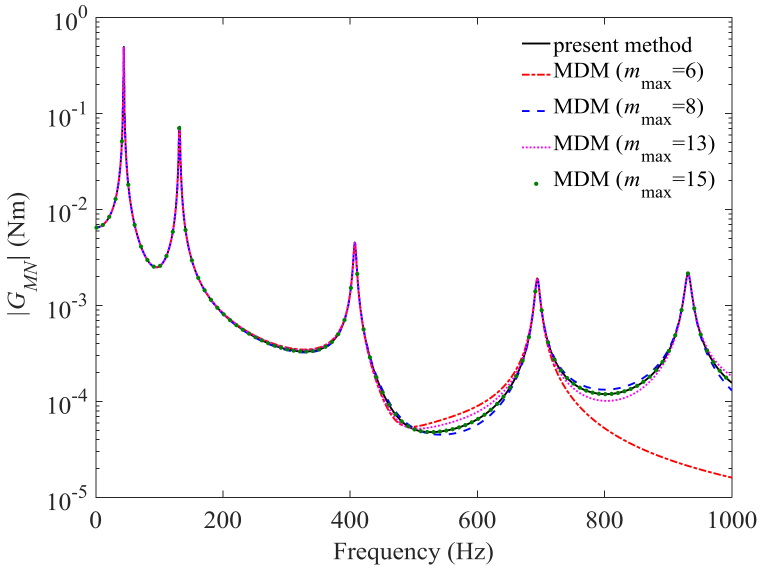

(a) $M = 1, N = 2$

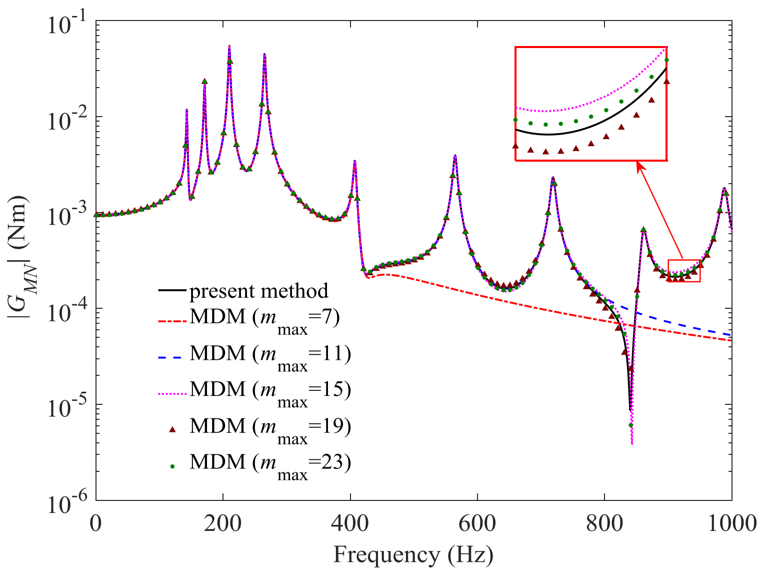

(b) $M = 4, N = 4$

Fig. 3 Magnitudes of the harmonic response function corresponding to the bending moment M_x at $(0.3L, 0.4\pi)$, calculated by the present method and the MDM with different modal truncations

The influences of the axial modal truncation $m_{\max}$ on harmonic response functions are studied, and the results are compared to those of the present method. As shown in Figs. 2 and 3, the truncation influences the responses significantly. With increasing frequency of the excitation, the number of modes required to obtain convergent solutions increases. Besides, with increasing orders M and N, the spatial distribution of the pressure varies considerably, and hence more modes are needed to ensure the accuracy of the results. Since the bending moment M_x is the derivative of the displacement w, many more modes are needed to obtain convergence on M_x than on w. Nevertheless, the present method is derived analytically and no truncation is introduced. Thus, compared with the MDM, the present method has the advantage of high accuracy in the solution of harmonic response functions.

The CPU times of the MDM with different modal truncations and the present method are listed in Table 2. The harmonic response functions corresponding to the displacement w are calculated at 400 points in the frequency range 1 to 1000 Hz, with a frequency step of 1 Hz. It can be observed that the CPU time of the MDM increases almost linearly with the increasing number of modes, while the present method keeps the same CPU time in all cases for the reason that no truncation is introduced. Thus, the present method has the advantage of high efficiency compared to the MDM, in the analysis of structures subjected to excitation with a wide frequency band, such as the TBL.

Table 2 CPU times of the MDM and the present method for different cases

$M=1$, $N=2$		$M=4$, $N=4$	
MDM, $m_{\max}=4$	49 s	MDM, $m_{\max}=7$	81 s
MDM, $m_{\max}=6$	73 s	MDM, $m_{\max}=9$	103 s
MDM, $m_{\max}=8$	90 s	MDM, $m_{\max}=11$	126 s
MDM, $m_{\max}=10$	113 s	MDM, $m_{\max}=15$	162 s
Present method	78 s	Present method	79 s

4.1.2 Influences of the axial compression on harmonic response functions

In order to study the influences of axial compressions on random responses of the cylindrical shell to the TBL, it is essential to firstly investigate the influences on harmonic response functions. According to the theory of elastic stability as shown in [28], the critical axial pressure of the cylindrical shell under consideration is about 9.427×10^6 N/m, which can be denoted as N_{cr}. When the compression exceeds the critical value, the cylindrical shell may lose stability. Therefore, the investigation of influences of axial compression on harmonic response functions is meaningful, even when the axial compression is below the critical value.

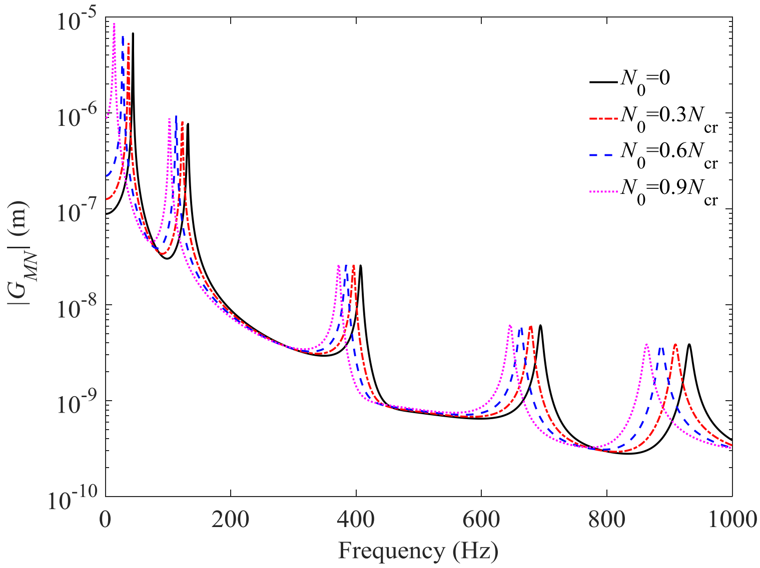

(a) $M = 1, N = 2$

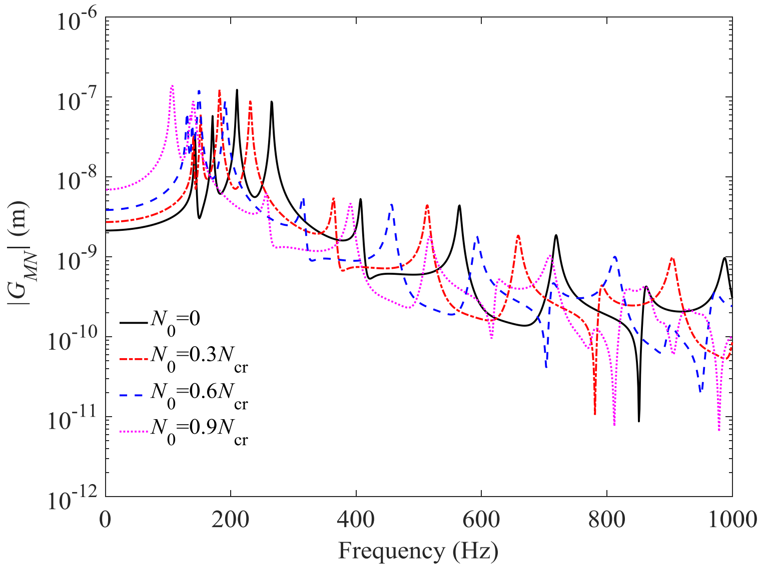

(b) $M = 4, N = 4$

Fig. 4 Magnitudes of the harmonic response function corresponding to the displacement w at $(0.3L, 0.4\pi)$ with different axial compressions

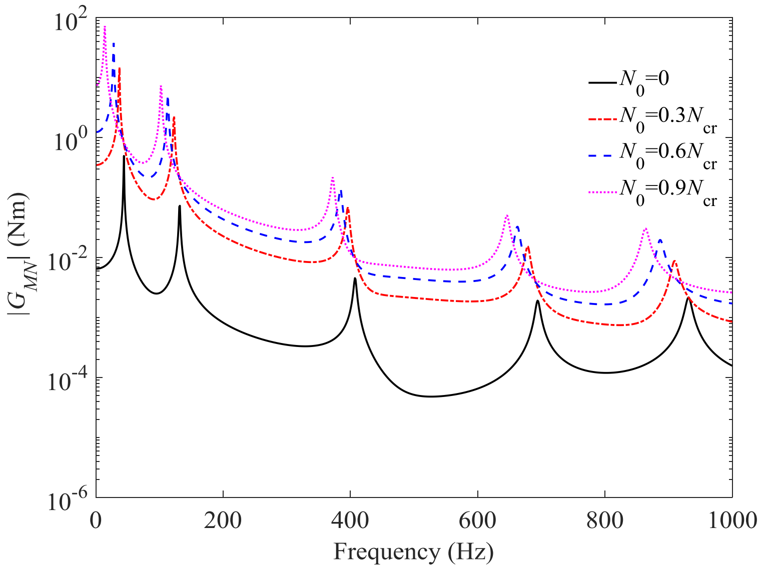

(a) $M = 1, N = 2$

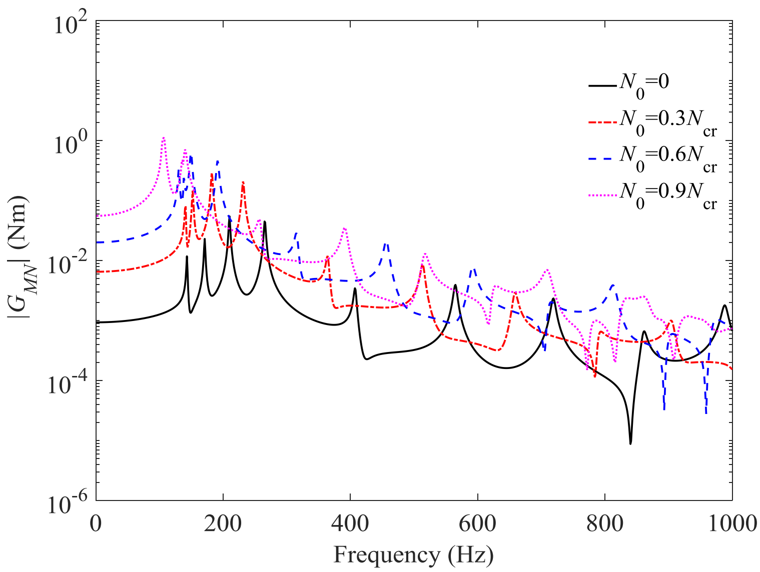

(b) $M = 4, N = 4$

Fig. 5 Magnitudes of the harmonic response function corresponding to the bending moment M_x at $(0.3L, 0.4\pi)$ with different axial compressions

The variation of harmonic response functions $G_{MN}(\mathbf{r},\omega)$ with the axial compression are shown in Figs. 4 and 5, which correspond to the displacement w and bending moment M_x at $x = 0.3L$ and $\theta = 0.4\pi$, respectively. It is seen that the peaks of $G_{MN}(\mathbf{r},\omega)$ shift to the left, as the axial compression reduces the natural frequencies. Also, for the modes of smaller circumferential order n, the axial compression has less influence on the natural frequencies. The amplitudes of the displacement w do not change much with increasing axial compression, whereas, those of the bending moment M_x change significantly. Hence it can be concluded that bending moment M_x is more sensitive to variation of the axial compression than the displacement w.

4.2 Random responses to the TBL

Random responses of the axially compressed cylindrical shell to the TBL are investigated by the present method in this section, following which the influences of the axial compression are discussed. The cross PSD of the TBL wall pressure developed by Corcos [1] is used here, with the parameters recommended in [11], i.e., $c_x = 0.15$, $c_\theta = 0.75$, $U_c = 75\,\mathrm{m/s}$. The auto PSD of point wall pressure $\Phi_{pp}(\omega)$ is a band-limited white noise with unit amplitude, and covers a frequency range from 1 to 1000 Hz.

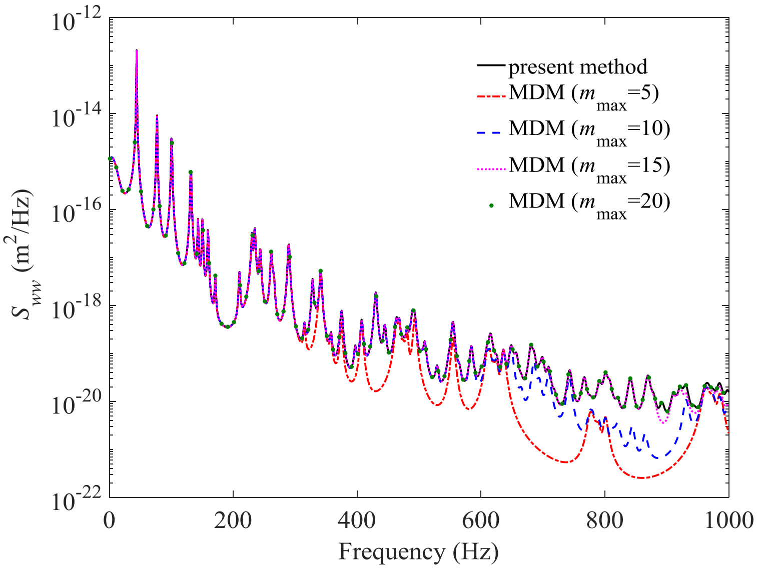

Fig. 6 Auto PSDs of the displacement w at $(0.3L, 0.4\pi)$, calculated by the present method and the MDM with different modal truncations

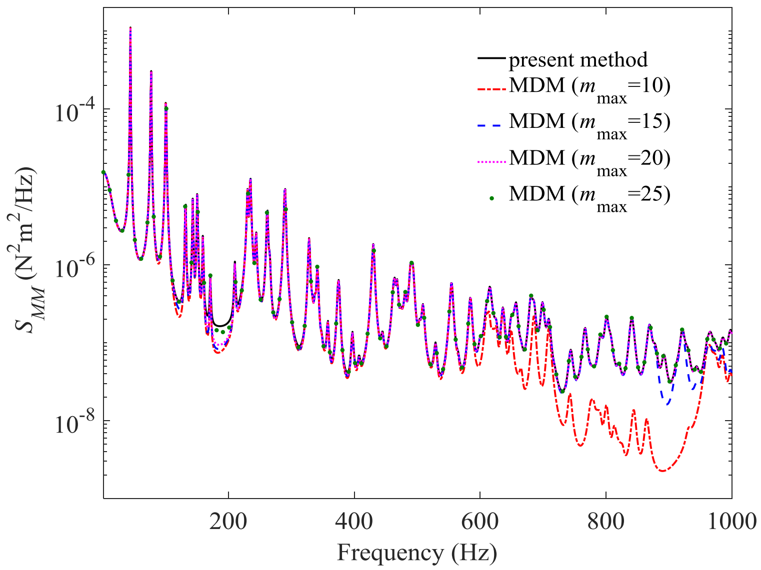

Fig. 7 Auto PSDs of the bending moment M_x at $(0.3L, 0.4\pi)$, calculated by the present method and the MDM with different modal truncations

4.2.1 Comparisons of the present method and MDM

Harmonic response functions obtained by the present method and the MDM were studied and compared in subsection 4.1.1, whereas in this subsection comparisons are given further for the random responses obtained by these two methods. A sufficiently large truncation of M and N, e.g. 100, is used here to ensure the convergence of the series, although this may bring some unnecessary computation. The convergence and truncation problems of the series will be studied in detail in the next subsection.

Auto PSDs of the displacement w at $(0.3L, 0.4\pi)$ calculated by the present method are examined and compared to those of the MDM with different modal truncations, as shown in Fig. 6. It is seen that results of the MDM converge to those of the present method with increasing number of modes. It is also observed that the higher the excitation frequency, the more modes are needed to obtain convergent results in the MDM. Fig. 7 shows the auto PSDs of the bending moment M_x at the same location, and similar phenomena to those of the displacement w can be observed. It is noted that the bending moment M_x needs more modes than the displacement w to obtain convergent random responses.

Auto PSDs of the displacement w and bending moment M_x along the axial and circumferential directions are shown in Figs. 8 and 9, respectively. Considering the spatial symmetry of responses, results are given in the range of 0 to $0.5L$ in the axial direction and 0 to 0.5π in the circumferential direction. For the convenience of displaying results, auto PSDs at only a typical frequency point, i.e. 600Hz, are examined and compared. As we can see from Figs. 8 and 9, with increasing modal truncation $m_{\max}$, results of the MDM converge to those of the present method. This tendency can be observed from results of both the displacement w and bending moment M_x, and in both axial and circumferential directions. This indicates that the present method can provide results with very high precision. In addition, in Figs. 8(a) and 9(a), if results of the present method are used as reference solutions and the maximum errors of the MDM are controlled within 1%, then at least 15 modes are needed for the calculation of the auto PSDs of the displacement w, while 28 for the bending moment M_x.

Auto PSDs of the displacement w and bending moment M_x along the axial and circumferential directions are shown in Figs. 8 and 9, respectively. Considering the spatial symmetry of responses, results are given in the range of 0 to $0.5L$ in the axial direction and 0 to 0.5π in the circumferential direction. For the convenience of displaying results, auto PSDs at only a typical frequency point, i.e. 600Hz, are examined and compared. It is seen from Figs. 8 and 9 that with increasing modal truncation $m_{\max}$, results of the MDM converge to those of the present method. This tendency can be observed from results of both the displacement w and bending moment M_x, and in both the axial and circumferential directions. This indicates that the present method can provide results with very high precision. In addition, in Figs. 8(a)

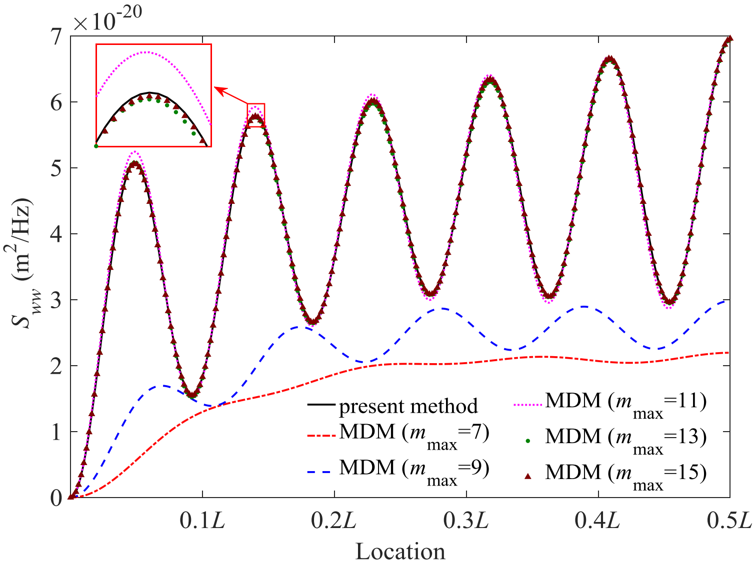

(a) The axial direction and $\theta = 0.4\pi$

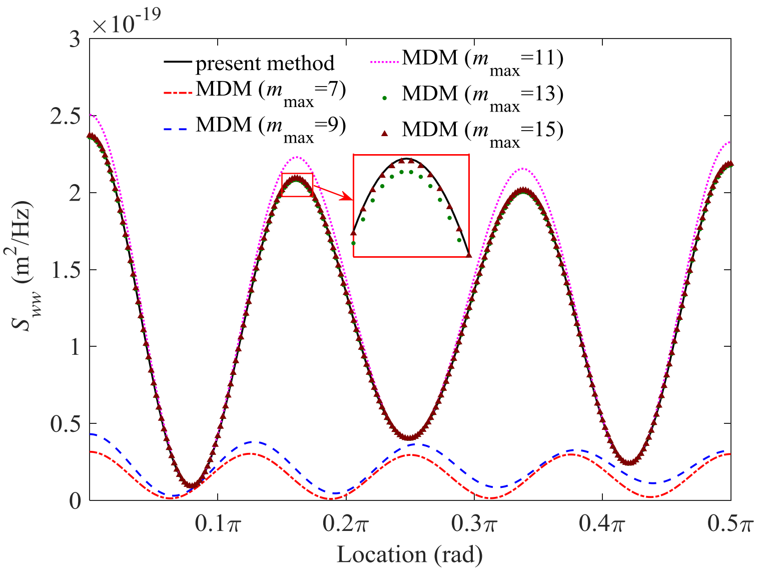

(b) The circumferential direction and $x = 0.3L$

Fig. 8 Auto PSDs of the displacement w along the axial and circumferential directions

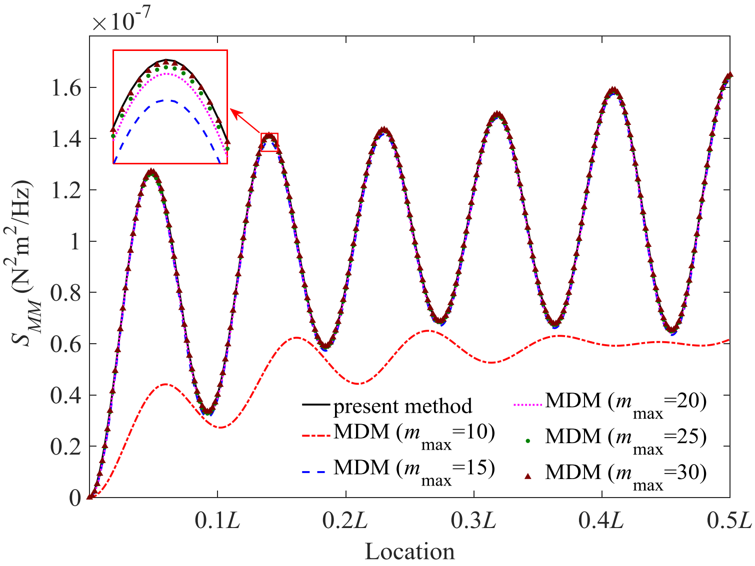

(a) The axial direction and $\theta = 0.4\pi$

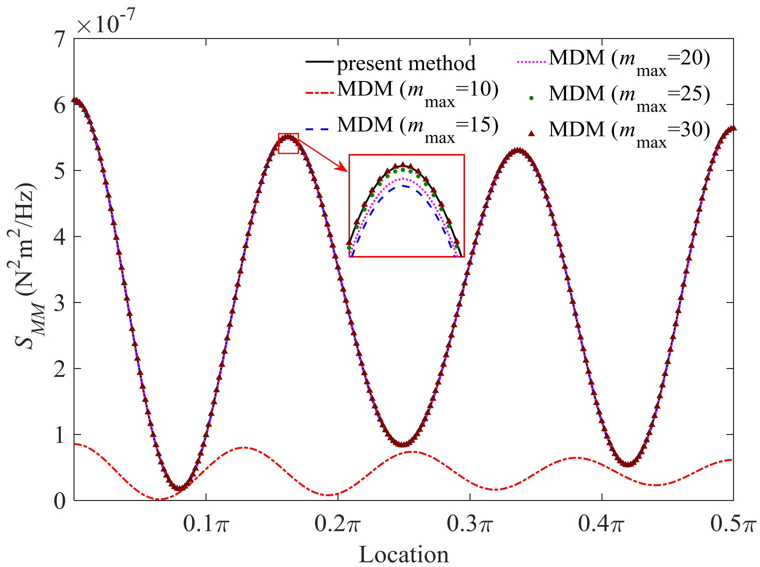

(b) The circumferential direction and $x = 0.3L$

Fig. 9 Auto PSDs of the bending moment M_x along the axial and circumferential directions and 9(a), if results of the present method are used as reference solutions and the maximum errors of the MDM are required to within 1%, then at least 15 modes are needed for calculation of the auto PSDs of the displacement w, and 28 for those of the bending moment M_x.

4.2.2 Convergence of the present method

As can be seen from Eq. (13), the cross PSD of the TBL is expanded as a Fourier series, whose convergence should be discussed. The truncations of the series in the axial and circumferential directions are denoted as $M_{\max}$ and $N_{\max}$, respectively. Figs. 10 and 11 give results for S_{ww} and S_{MM} with different truncations, representing the auto PSDs of the displacement w and bending moment M_x of the cylindrical shell. It should be noted that when the convergence of one direction is studied, a sufficiently large truncation in the other direction is considered to ensure the convergence of the solutions. As shown in Figs. 10 and 11, the results are convergent with increasing truncations of the series in both directions. For higher frequencies, larger truncation is needed to obtain convergent results. Also, the convergence of S_{MM} is significantly slower than that of S_{ww}. This phenomenon is similar to the convergence of the MDM.

The convergence of the solutions at each frequency is studied further. Defining the truncation error as

$$\varepsilon(\Theta) = \frac{\mathrm{Res}(\Theta) - \mathrm{Res}(\Theta - 1)}{\mathrm{Res}(\Theta)} \times 100\% \tag{39}$$

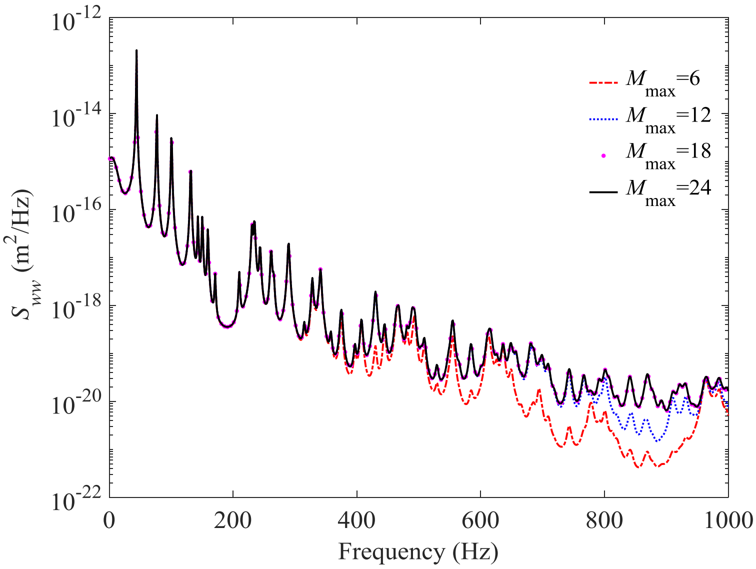

(a) $M_{\max}$

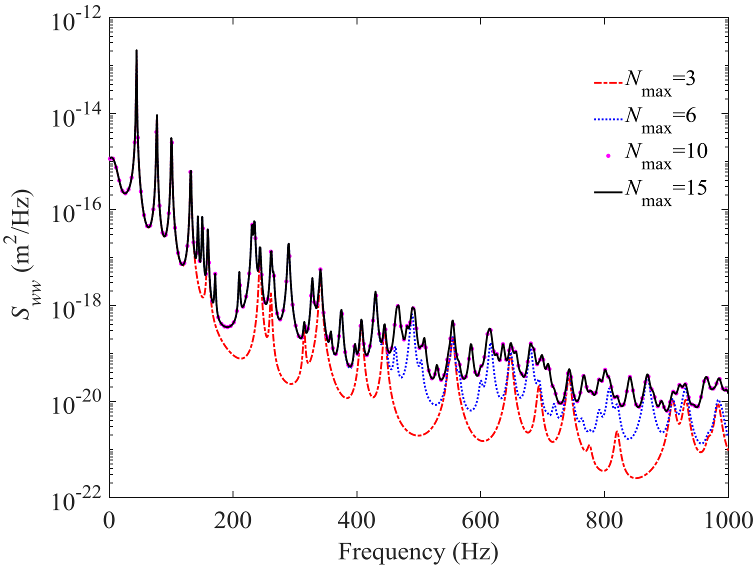

(b) $N_{\max}$

Fig. 10 Auto PSDs of the displacement w at $(0.3L, 0.4\pi)$ with different truncations in axial and circumferential directions

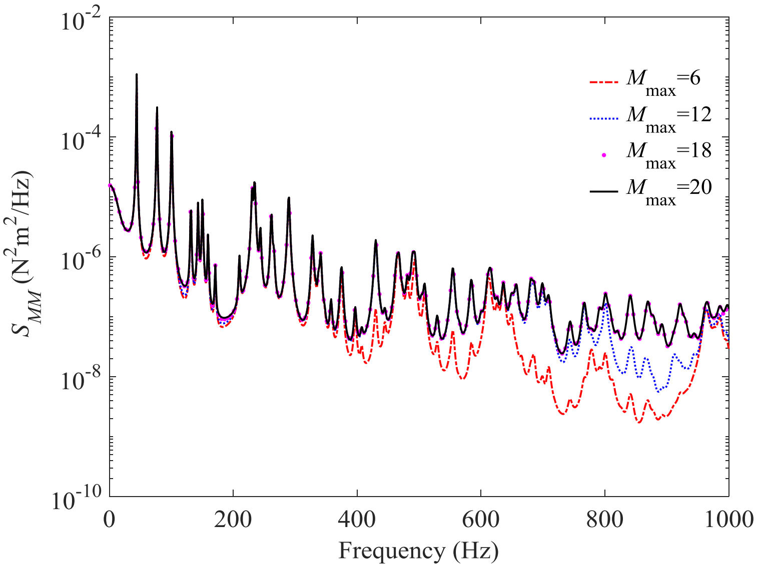

(a) $M_{\max}$

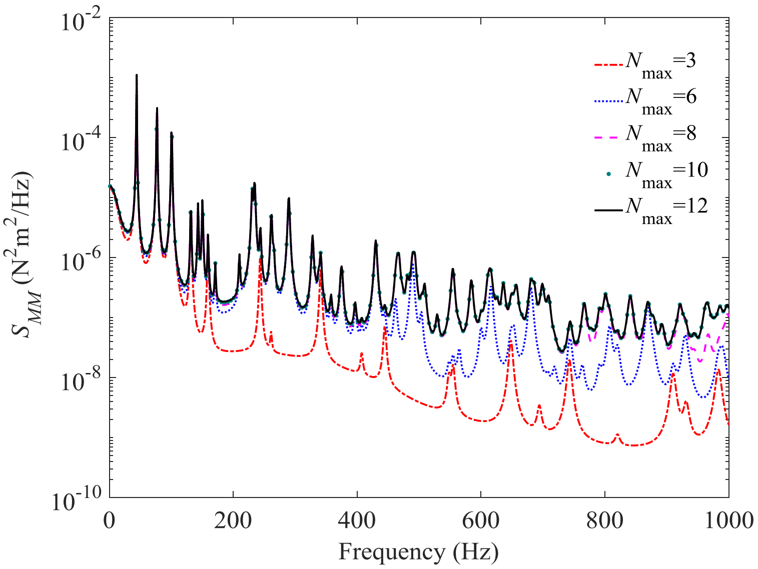

(b) $N_{\max}$

Fig. 11 Auto PSDs of the bending moment M_x at $(0.3L, 0.4\pi)$ with different truncations in axial and circumferential directions

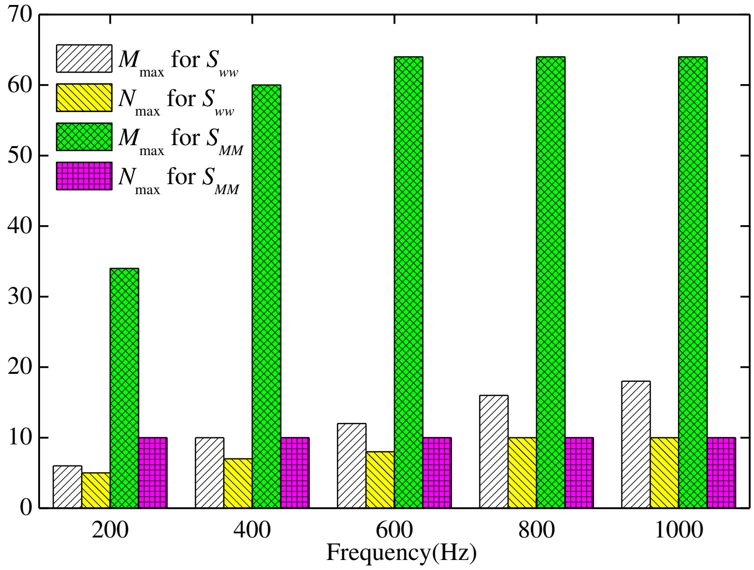

Fig. 12 Convergence diagram for S_{ww} and S_{MM}

where $\mathrm{Res}(\Theta)$ is the solution with respect to Θ terms, and Θ can be $M_{\max}$ or $N_{\max}$. It is assumed that the solution is convergent if $\varepsilon(\Theta)$ is smaller than 1%. According to the above rule, the convergence of the solutions in a frequency range between 1 and 1000 Hz is studied, and some of the results are presented in Fig. 12. It is seen that more terms are needed to ensure the convergence of the solutions at higher frequencies. Also, the convergence in the axial direction is much slower than that in the circumferential direction.

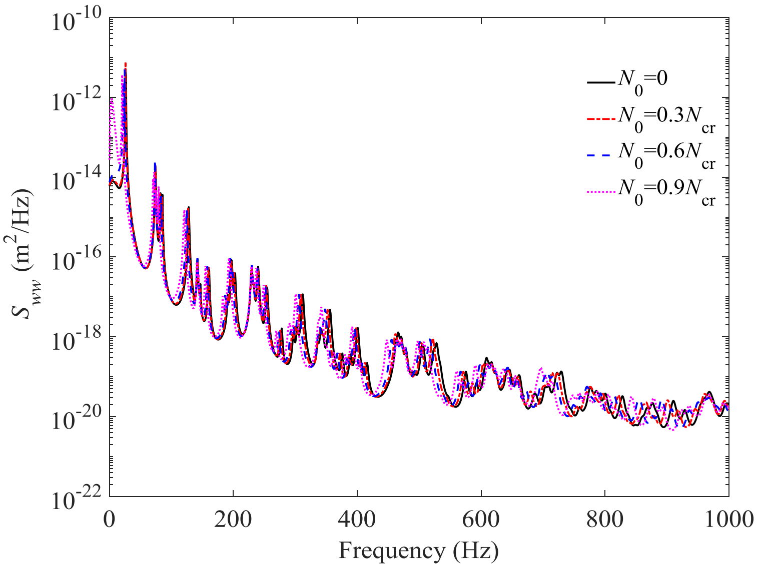

Fig. 13 Auto PSDs of the displacement w at $(0.3L, 0.4\pi)$ with different axial compressions

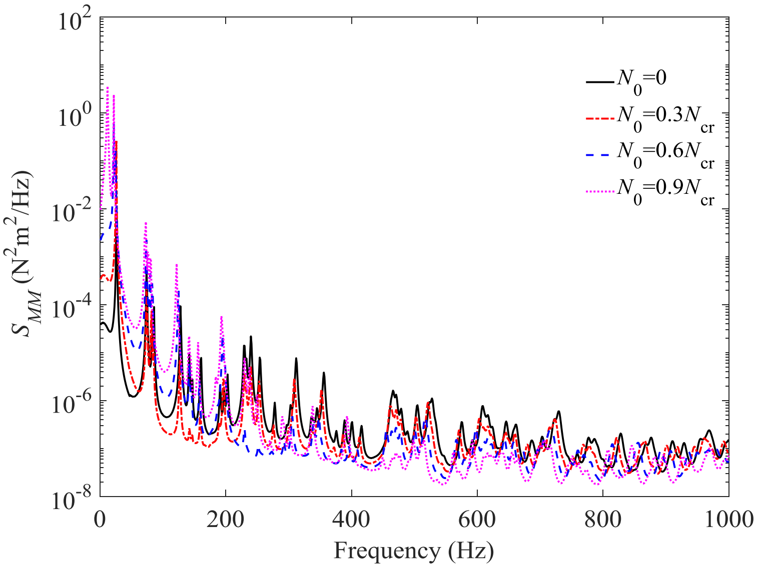

Fig. 14 Auto PSDs of the bending moment M_x at $(0.3L, 0.4\pi)$ with different axial compressions

4.2.3 Influences of the axial compression on random responses

The influences of axial compression on the random responses of the cylindrical shell subjected to the TBL are investigated. The boundary condition with free-free ends is considered here. Like the investigation on harmonic response functions in section 4.1.2, the axial compression is below the critical value, which equals -9.7×10^5 N/m for the case of free-free ends. The auto PSDs of the displacement w and bending moment M_x, at $(0.3L, 0.4\pi)$ with different axial compression are given in Figs. 13 and 14. It can be seen that the variation of the axial compression has a great influence on both S_{ww} and S_{MM}. As the axial compression increases, the peaks of PSDs shift to the left. Also, S_{MM} is more sensitive to the variation of the axial compression than S_{ww}.

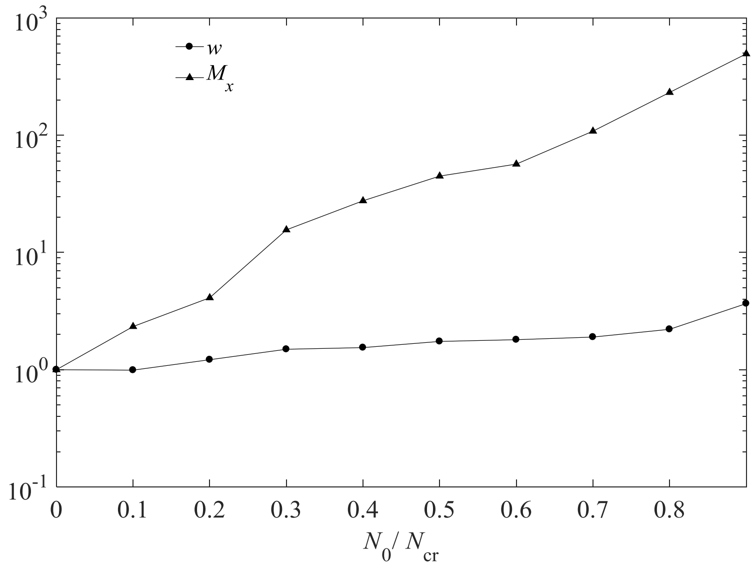

Fig. 15 Mean square values of the displacement and bending moment at $(0.3L, 0.4\pi)$ with different axial compressions, normalized by the results without axial compression

Fig. 15 shows the mean square values of the displacement w and bending moment M_x with different axial compressions. For convenience of illustration, all results are normalized with respect to those without axial compression. It can be seen that the mean square values increase with the increasing axial compression. Also, the influence of axial compression on the mean square values of the bending moment is much more significant than that on the displacement.

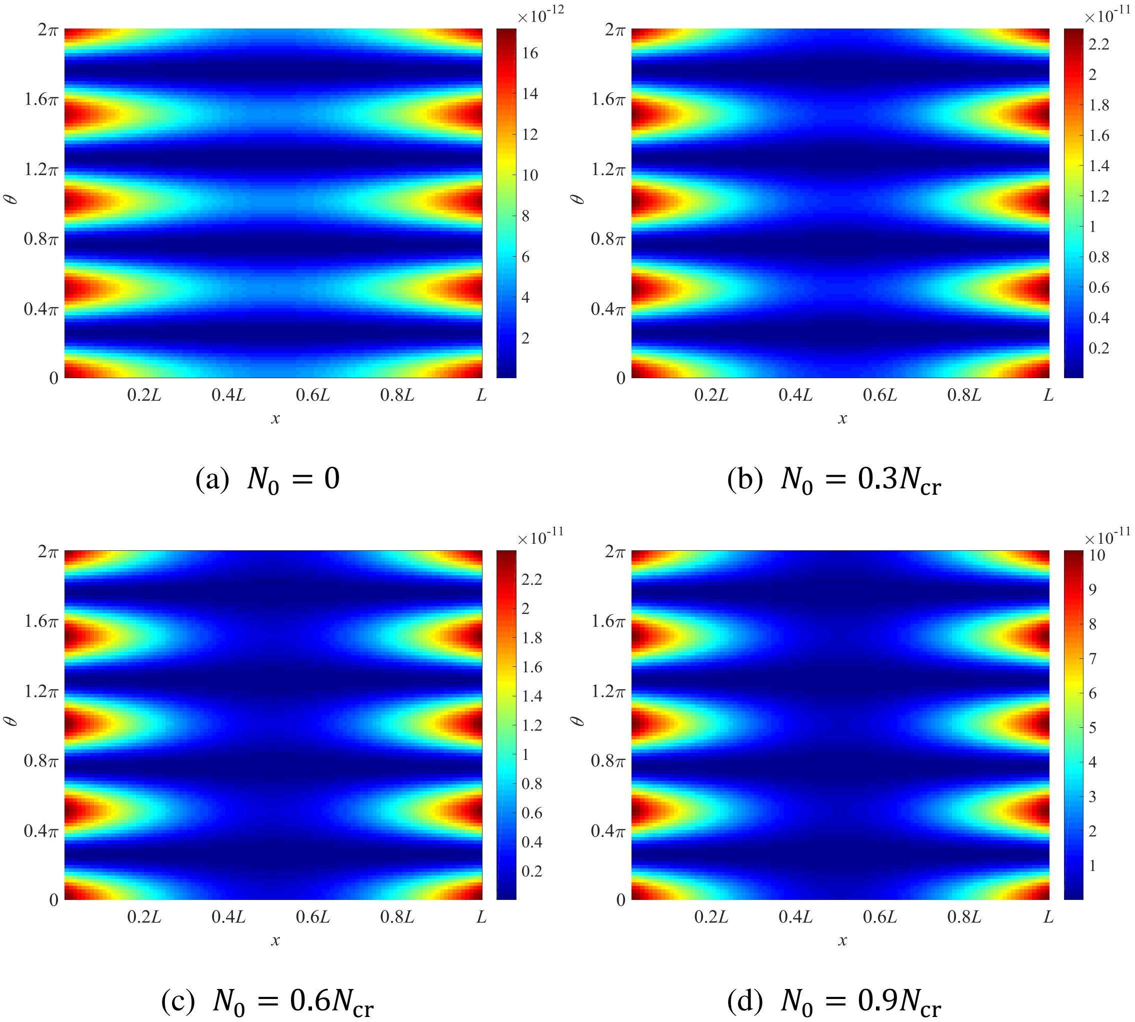

(a) $N_0 = 0$ (b) $N_0 = 0.3N_{\mathrm{cr}}$

(c) $N_0 = 0.6N_{\mathrm{cr}}$ (d) $N_0 = 0.9N_{\mathrm{cr}}$

Fig. 16 Evolution of the distribution of the mean square value of the displacement w with different axial compressions

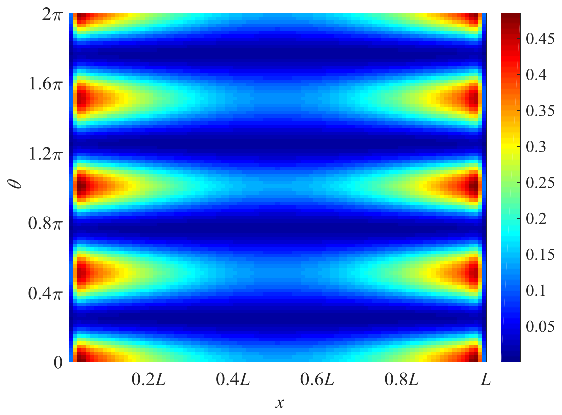

(a) $N_0 = 0$

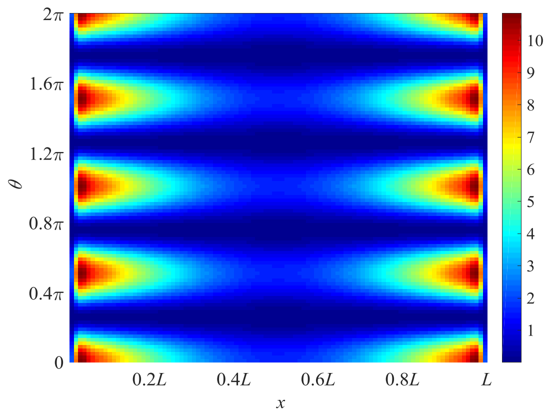

(b) $N_0 = 0.3N_{\rm cr}$

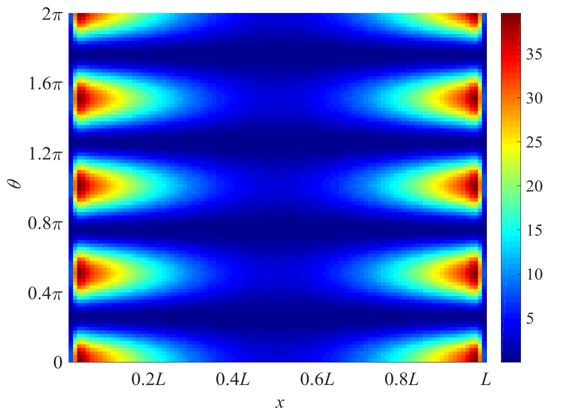

(c) $N_0 = 0.6N_{\rm cr}$

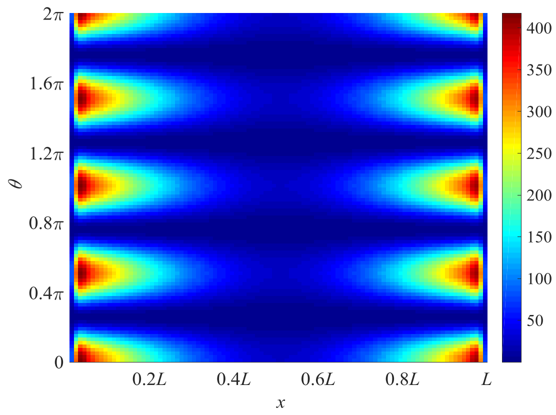

(d) $N_0 = 0.9N_{\rm cr}$

Fig. 17 Evolution of the distribution of the mean square value of the bending moment M_x with different axial compressions

Figs. 16 and 17 show the distributions of the mean square values of the displacement w and bending moment M_x, respectively. It can be seen that the amplitudes of the mean square values increase significantly with axial compression, while the distributions over the cylindrical shell do not change much. Moreover, the distributions are similar to the modal shape with order $m = 1$ and $n = 2$ which corresponds to the smallest natural frequency. This is because the natural frequencies are modified by the axial compression, but the corresponding mode shapes are still the same as those without axial compression.

5 Conclusions

A method based on the symplectic duality system is presented to predict the random responses of the axially compressed cylindrical shell subjected to the TBL. The cross PSD of the TBL is expressed as a Fourier series. Then the problem of structures subjected to a random pressure field like the TBL is reduced to the solution of harmonic response functions. A symplectic method is developed to obtain the harmonic response functions analytically. Firstly, harmonic response functions with different wavenumbers are calculated by the present method and the MDM. The results show that the present method is efficient and accurate compared to the MDM. Then influences of the axial compression on the harmonic response functions are discussed, and it is indicated that the axial compression has more influence on the harmonic response functions with bigger wavenumbers. Secondly, random responses of the cylindrical shell to the TBL are calculated and compared to those of the MDM, and then the convergence problems induced by Fourier series expansion are discussed. It is shown that the convergence in the axial direction is much slower than that in the circumferential direction, while the convergence of the bending moment is slower than that of the displacement. Finally, the influences of axial compression on the random responses of the cylindrical shell subjected to the TBL are investigated. It is concluded that axial compression has a significant influence on the amplitude of random responses, and that the bending moment is more sensitive than the displacement to the variation of the axial compression. However, the axial compression has little influence on the spatial distribution of random responses.

Acknowledgments

The authors are grateful for support under grants from the National Science Foundation of China (11672060), the National Basic Research Program of China (2014CB046803), and the Cardiff University Advanced Chinese Engineering Centre.

Appendix Nonzero elements in operator matrix $\mathbf{H}$

The nonzero elements in the operator matrix $\mathbf{H}$, as shown in Eq. (24) are

$$\mathbf{H}_{12} = -\mathbf{H}_{65} = -\frac{\nu K}{(K - N_0)R}\frac{\partial}{\partial\theta} \tag{A1}$$

$$\mathbf{H}_{13} = -\mathbf{H}_{75} = -\frac{\nu K}{(K - N_0)R} \tag{A2}$$

$$\mathbf{H}_{15} = \frac{1}{K - N_0} \tag{A3}$$

$$\mathbf{H}_{21} = -\mathbf{H}_{56} = \frac{KR(1-\nu)}{(KR^2 + D)(\nu - 1) + 2N_0R^2}\frac{\partial}{\partial\theta} \tag{A4}$$

$$\mathbf{H}_{24} = -\mathbf{H}_{68} = \frac{2D(1-\nu)}{(KR^2 + D)(\nu - 1) + 2N_0R^2}\frac{\partial}{\partial\theta} \tag{A5}$$

$$\mathbf{H}_{26} = \frac{2R^2}{(KR^2 + D)(\nu - 1) + 2N_0R^2} \tag{A6}$$

$$\mathbf{H}_{34} = -\mathbf{H}_{87} = -1 \tag{A7}$$

$$\mathbf{H}_{42} = -\mathbf{H}_{68} = -\frac{\nu}{R^2}\frac{\partial}{\partial\theta} \tag{A8}$$

$$\mathbf{H}_{43} = -\mathbf{H}_{78} = -\frac{N_0}{D} + \frac{\nu}{R^2}\frac{\partial^2}{\partial\theta^2} \tag{A9}$$

$$\mathbf{H}_{48} = \frac{1}{D} \tag{A10}$$

$$\mathbf{H}_{51} = -\rho h\omega^2 + \frac{[2N_0R^2 + D(\nu - 1)](\nu - 1)K}{2R^2[(KR^2 + D)(\nu - 1) + 2N_0R^2]}\frac{\partial^2}{\partial\theta^2} \tag{A11}$$

$$\mathbf{H}_{54} = \mathbf{H}_{81} = \frac{-(\nu - 1)^2DK}{R[(KR^2 + D)(\nu - 1) + 2N_0R^2]}\frac{\partial^2}{\partial\theta^2} \tag{A12}$$

$$\mathbf{H}_{56} = \frac{-KR(1 - \nu)}{(KR^2 + D)(\nu - 1) + 2N_0R^2}\frac{\partial}{\partial\theta} \tag{A13}$$

$$\mathbf{H}_{62} = \rho h\omega^2 - \frac{(R^2K^2 + DK - DN_0)(\nu^2 - 1) + R^2N_0K}{(K - N_0)R^4}\frac{\partial^2}{\partial\theta^2} \tag{A14}$$

$$\mathbf{H}_{63} = \mathbf{H}_{72} = -\frac{(\nu^2 - 1)K^2 + N_0(\nu + 1)K - \nu N_0^2}{(K - N_0)R^2}\frac{\partial}{\partial\theta} + \frac{D(\nu^2 - 1)}{R^4}\frac{\partial^3}{\partial\theta^3} \tag{A15}$$

$$\mathbf{H}_{73} = -\rho h\omega^2 + \frac{(1 - \nu^2)K^2 - N_0K}{(K - N_0)R^2} + \frac{(1 - \nu^2)D}{R^4}\frac{\partial^4}{\partial\theta^4} \tag{A16}$$

$$\mathbf{H}_{84} = \frac{2D(\nu - 1)(K\nu - K + 2N_0)}{(KR^2 + D)(\nu - 1) + 2N_0R^2}\frac{\partial^2}{\partial\theta^2} \tag{A17}$$

References

[1] Corcos G M. The structure of the turbulent pressure field in boundary-layer flows. Journal of Fluid Mechanics, 1964, 18(3): 353-378.

[2] Efimtsov B M. Characteristics of the field of turbulent wall pressure-fluctuations at large Reynolds-numbers. Soviet Physics Acoustics, 1982, 28(4): 289-292.

[3] Smol'yakov A V, Tkachenko V M. Measurement of turbulent fluctuations. Berlin Heidelberg: Springer, 1983.

[4] Graham W R. A comparison of models for the wavenumber-frequency spectrum of turbulent boundary layer pressures. Journal of Sound and Vibration, 1997, 206(4): 541-565.

[5] Lakis A A, Paidoussis M P. Prediction of the response of a cylindrical shell to arbitrary or boundary-layer-induced random pressure fields. Journal of Sound and Vibration, 1972, 25(1): 1-27.

[6] Esmailzadeh M, Lakis A A, Thomas M, Marcouiller L. Prediction of the response of a thin structure subjected to a turbulent boundary-layer-induced random pressure field. Journal of Sound and Vibration, 2009, 328(1): 109-128.

[7] Esmailzadeh M, Lakis A A. Response of an open curved thin shell to a random pressure field arising from a turbulent boundary layer. Journal of Sound and Vibration, 2012, 331(2): 345-364.

[8] Montgomery J M. Modeling of aircraft structural-acoustic response to complex sources using coupled FEM-BEM analyses. 10th AIAA/CEAS Aeroacoustics Conference, Manchester, United Kingdom, May 10-12, 2004-2822: 266-274.

[9] Newland D E. An introduction to random vibrations, spectral and wavelet analysis. New York: Longman, 2012.

[10] Lin Y K. Probabilistic theory of structural dynamics. New York: McGraw-Hill, 1967.

[11] Durant C, Robert G, Filippi P J T, Mattei P O. Vibroacoustic response of a thin cylindrical shell excited by a turbulent internal flow: comparison between numerical prediction and experimentation. Journal of Sound and Vibration, 2000, 229(5): 1115-1155.

[12] Zhou J, Bhaskar A, Zhang X. Sound transmission through double cylindrical shells lined with porous material under turbulent boundary layer excitation. Journal of Sound and Vibration, 2015, 357: 253-268.

[13] Liu B. Noise radiation of aircraft panels subjected to boundary layer pressure fluctuations. Journal of Sound and Vibration, 2008, 314(3): 693-711.

[14] Maury C, Gardonio P, Elliott S J. A wavenumber approach to modelling the response of a randomly excited panel, Part I: General theory. Journal of Sound and Vibration, 2002, 252(1): 83-113.

[15] Maury C, Gardonio P, Elliott S J. A wavenumber approach to modelling the response of a randomly excited panel, Part II: Application to aircraft panels excited by a

turbulent boundary layer. Journal of Sound and Vibration, 2002, 252(1): 115-139.

[16] De Rosa S, Franco F. Exact and numerical responses of a plate under a turbulent boundary layer excitation. Journal of Fluids and Structures, 2008, 24(2): 212-230.

[17] Birgersson F, Ferguson N S, Finnveden S. Application of the spectral finite element method to turbulent boundary layer induced vibration of plates. Journal of Sound and Vibration, 2003, 259(4): 873-891.

[18] Dahlberg T. The effect of modal coupling in random vibration analysis. Journal of Sound and Vibration, 1999, 228(1): 157-176.

[19] Soedel W, Qatu M S. Vibrations of shells and plates. New York: Marcel Dekker, 2004.

[20] Lü C F, Chen W Q. Comment on "Exact dynamic analysis of space structures using Timoshenko beam theory". AIAA Journal, 2006, 44(6): 1372-1373.

[21] Birgersson F, Finnveden S, Robert G. Modelling turbulence-induced vibration of pipes with a spectral finite element method. Journal of Sound and Vibration, 2004, 278(4): 749-772.

[22] Langley R S. Application of the dynamic stiffness method to the free and forced vibrations of aircraft panels. Journal of Sound and Vibration, 1989, 135(2): 319-331.

[23] Zhong W X. Duality system in applied mechanics and optimal control, Boston: Kluwer Academic Publishers, 2004.

[24] Xu X S, Ma Y, Lim C W, Chu H J. Dynamic buckling of cylindrical shells subject to an axial impact in a symplectic system. International Journal of Solids and Structures,

2006, 43(13): 3905-3919.

[25] Lim C W, Lü C F, Xiang Y, Yao W. On new symplectic elasticity approach for exact free vibration solutions of rectangular Kirchhoff plates. International Journal of Engineering Science, 2009, 47(1): 131-140.

[26] Ma Y B, Zhang Y H, Kennedy D. A symplectic analytical wave based method for the wave propagation and steady state forced vibration of rectangular thin plates. Journal of Sound and Vibration, 2015, 339: 196-214.

[27] Ma Y B, Zhang Y H, Kennedy D. Energy flow analysis of mid-frequency vibration of coupled plate structures with a hybrid analytical wave and finite element model. Computers & Structures, 2016, 175: 1-14.

[28] Timoshenko S P, Gere J M. Theory of elastic stability. New York: McGraw-Hill, 2009.

Table captions

Table 1 Natural frequencies of the cylindrical shell without axial compression

Table 2 CPU times of the MDM and the present method for different cases

Figure captions

Fig. 1 Schematic of an axially compressed cylindrical shell

Fig. 2 Magnitudes of the harmonic response function corresponding to the displacement w at $(0.3L, 0.4\pi)$, calculated by the present method and the MDM with different truncations

Fig. 3 Magnitudes of the harmonic response function corresponding to the bending moment M_x at $(0.3L, 0.4\pi)$, calculated by the present method and the MDM with different modal truncations

Fig. 4 Magnitudes of the harmonic response function corresponding to the displacement w at $(0.3L, 0.4\pi)$ with different axial compressions

Fig. 5 Magnitudes of the harmonic response function corresponding to the bending moment M_x at $(0.3L, 0.4\pi)$ with different axial compressions

Fig. 6 Auto PSDs of the displacement w at $(0.3L, 0.4\pi)$, calculated by the present method and the MDM with different modal truncations

Fig. 7 Auto PSDs of the bending moment M_x at $(0.3L, 0.4\pi)$, calculated by the present method and the MDM with different modal truncations

Fig. 8 Auto PSDs of the displacement w along the axial and circumferential directions

Fig. 9 Auto PSDs of the bending moment M_x along the axial and circumferential directions

Fig. 10 Auto PSDs of the displacement at $(0.3L, 0.4\pi)$ with different truncations in axial and circumferential directions

Fig. 11 Auto PSDs of the bending moment at $(0.3L, 0.4\pi)$ with different truncations in axial and circumferential directions

Fig. 12 Convergence diagram for S_{ww} and S_{MM}

Fig. 13 Auto PSDs of the displacement at $(0.3L, 0.4\pi)$ with different axial compressions

Fig. 14 Auto PSDs of the bending moment at $(0.3L, 0.4\pi)$ with different axial compressions

Fig. 15 Mean square values of the displacement and bending moment at $(0.3L, 0.4\pi)$ with different axial compressions, normalized by the results without axial compression

Fig. 16 Evolution of the distribution of the mean square value of the displacement with different axial compressions

Fig. 17 Evolution of the distribution of the mean square value of the bending moment with different axial compressions